Ultrasound in Med. & Biol., Vol. 36, No. 4, pp. 623–636, 2010

0301-5629/10/$–see front matter

ELSEVIER

doi:10.1016/j.ultrasmedbio.2010.01.011

● *Original Contribution*

ESTIMATION OF AVERAGE SPEED OF SOUND USING DECONVOLUTION OF MEDICAL ULTRASOUND DATA

Ho-Chul Shin, Richard Prager, Henry Gomersall, Nick Kingsbury, Graham Treece, and Andrew Gee

Department of Engineering, University of Cambridge, Cambridge, United Kingdom

(*Received* 15 *April* 2009; *revised* 8 *January* 2010; *in final form* 28 *January* 2010)

Abstract—In diagnostic ultrasound imaging the speed of sound is assumed to be 1540 m/s in soft tissues. When the actual speed is different, the mismatch can lead to distortions in the acquired images and so reduce their clinical value. Therefore, the estimation of the true speed has been pursued not only because it enables image correction but also as a way of tissue characterisation. In this article, we present a novel way to measure the average speed of sound concurrently with performing image enhancement by deconvolution. This simultaneous capability, based on a single acquisition of ultrasound data, has not been reported in previous publications. Our algorithm works by conducting non-blind deconvolution of the reflection data with point-spread functions based on different speeds of sound. Using a search strategy, we select the speed that produces the best-possible restoration. The deconvolution operates on the beamformed uncompressed radio-frequency data, without any need to modify the hardware of the ultrasound machine. A conventional handling of the transducer array is all that is required in the data acquisition part of our proposed method: the data can be collected freehand, unlike most other estimation methods. We have tested our algorithm with simulations, *in vitro* phantoms with known and unknown speeds and *in vivo* scans. The estimation error was found to be +0.19 ± 8.90 m/s (mean ± standard deviation) for *in vitro* in-house phantoms whose speeds were also measured independently. In addition to the speed estimation, our method has also proved to be capable of simultaneously producing a better restoration of ultrasound images than deconvolution by an assumed speed of 1540 m/s, when this assumption is incorrect. (E-mail: hs338@cam.ac.uk) © **2010 World Federation for Ultrasound in Medicine & Biology.**

Key Words: **Medical ultrasound, Non-blind deconvolution, Point-spread function, Speed of sound, Sound estimation.**

INTRODUCTION AND LITERATURE

Conventional ultrasound imaging assumes the speed of sound is 1540 m/s in soft tissue for the design of the beamforming delay pattern. This potentially leads to degradation of B-mode images and data restored by non-blind deconvolution when the actual speed of sound is different. The effects of errors in the sound speed, such as degraded spatial resolution, have been widely reported and some of the consequences have been quantified (Anderson et al. 2000).

Research on the speed of sound in the medical ultrasound community has mainly focused on two aspects: estimation (in the context of tissue characterisation) and correction (in the context of image perception). In most previous publications, both topics have been dealt with separately. In this article, we propose a method of measuring an average speed of sound in broadly homogeneous tissue with simultaneous image correction if the estimated speed is different from 1540 m/s. We present this algorithm in a framework of ultrasound data deconvolution (Ng et al. 2006, 2007; Shin et al. 2009), which is the process of reducing image blurring and noise using prior knowledge of the blurring function and noise distribution. Therefore, our approach to speed correction in the restored ultrasound data is different from the techniques employed previously in original B-mode images.

Initially, the speed of medical ultrasound was estimated using transmission methods, which measured the time taken while a pulse propagated between a transmitter and a receiver. Clinical applications were limited to the breast (Hayashi et al. 1988). Robinson et al. (1991) carried out an extensive review of pulse-echo sound-speed estimation techniques. Nine methods in three categories were examined in detail. Despite using pulse-echo

Address correspondence to: Ho-Chul Shin, Department of Engineering, University of Cambridge, Trumpington Street, Cambridge, CB2 1PZ, United Kingdom. E-mail: hs338@cam.ac.uk

techniques, most of the reviewed methods were designed to employ multiple apertures of ultrasound transducers: one for transmission and the rest for reception and the use of paired transducer apertures increased the system complexity. A precise geometric relation needs to be established between transducers and scanned regions-of-interest (Robinson et al. 1991) and this is vulnerable to estimation errors. In some methods (Robinson et al. 1991), a pair of transducer elements in a single linear array can replace a pair of transducer apertures, which, however, may suffer a low signal-to-noise ratio. Several methods reviewed by Robinson et al. (1991) were also limited to tissues, which have recognisable features to have a geometric relation well-defined. However, there were a couple of methods that worked using a single transducer aperture. The transaxial compression technique (Ophir and Yazdi 1990; Robinson et al. 1991) is among them but it involves a precise movement of a transducer that compresses the tissue surface plus the acquisition of multiple scans after compression. A least-squares linear fit is made between known tissue-compression depths and arrival times of echoes and the slope of this linear fit is an estimate of the sound speed. In another technique called the dynamic focus method (Hayashi et al. 1988), the speed of sound in the ultrasonic beamformer is varied by operators until the clearest image is obtained, which is not systematic and effectively requires multiple scans.

Anderson and Trahey (1998) estimated the average speed of sound in a homogeneous medium based on the quadratic best-fit of the one-way geometric delay pattern acquired on individual elements of a transducer array. Their method is closely related to those used in exploration seismology and only requires a single scan of a medium with a single transducer array. Its accuracy and precision are cited in later sections for comparison purposes with our approach. They also showed that phase errors associated with wrong average sound speed are as much as two times bigger in dynamic-receive focus than fixed-receive focus systems. Sound-speed estimation is therefore potentially more valuable to dynamic-receive focus machines. Later, such a time-delay pattern was also exploited by Pereira et al. (2002) with application to bovine livers but an additional hydrophone was required as a receiver. Recently, an image registration technique was explored to estimate the speed of sound (Krücker et al. 2004). A single transducer array was used but multiple scans were necessary following beam steering.

Most of the methods reviewed by Robinson et al. (1991) produce the average speed of sound in the scanned tissues. Only a handful of them were capable of local speed estimation and the demonstration of a mapping capability was very rare. Kondo et al. (1990) reported mapping of *in vivo* local sound-speed estimation. But, they conceded that an exact measurement of local sound speed was difficult.

There is not much literature that describes a perceptual improvement in images associated with estimating the speed of sound. Jellins and Kossoff (1973) demonstrated an enhanced resolution in B-mode images by electronically matching the average sound speed in breasts to that in surrounding coupling water. It was observed that the compensation of linear displacement alone led to an improvement without correcting errors associated with refraction angles along the boundary between water and breast. Napolitano et al. (2006) showed B-mode images of *in vitro* and *in vivo* scans after estimation and subsequent correction of the speed. Although they proposed an automated algorithm (unlike the operator-dependent method by Hayashi et al. 1988) by analysing the spatial frequency information in a B-mode image, the estimation was carried out by acquiring many images with various trial sound speeds. This was achieved by adjusting the beamformer time delays in the ultrasound machine.

Incorrect assumptions about the ultrasound speed in inhomogeneous overlying tissue lead to degraded medical ultrasound images. This problem is often caused by the skin/fat/muscle structure. There are a number of studies in the literature that address it through the correction of phase aberration (Anderson and Trahey 1998). Numerous methods have been proposed (Flax and O'Donnell 1988; Nock et al. 1989; Ng et al. 1994, 1997). They differ from one another in how they estimate the aberration profile across the transducer elements but most of them share the idea of changing the time delays in individual elements according to the estimated aberration profile. During the profile estimation process, many techniques require multiple acquisitions of the radio-frequency (RF) signal. Most of all, previous work on phase aberration has focused on the reduction of perceived image degradation. In addition to aberration attributed to local inhomogeneity, Anderson and Trahey (1998) reported that a part of the phase aberration phenomenon can be caused by a discrepancy in the assumed and the true average speed in tissue. Therefore, sound speed estimation can contribute to a part of aberration correction.

In the category of medical ultrasound image restoration, uncertainty in the speed of sound especially for *in vivo* applications may be addressed through blind deconvolution (Abeyratne et al. 1995; Adam and Michailovich 2002; Michailovich and Adam 2004; Taxt 2001; Taxt and Strand 2001; Wan et al. 2003), in which a point-spread function (PSF) based on an actual speed of sound is estimated directly from the RF ultrasound data to be restored. However, blind approaches are not used to estimate the speed of sound because it is not easily parameterised. In contrast, non-blind deconvolution can make such an estimation possible due to the parameterisation of the sound speed in the PSF.

Our research group has recently studied the effects of uncertainty in the PSF on non-blind deconvolution (Shin et al. 2009). The parameters of an ultrasound imaging PSF have been systematically investigated. In total, six parameters were examined: uncertainty in the ultrasound machine was analysed by varying the axial depth of lateral focus and the radius of elevational focus alongside the height and width of the transducer elements. Sensitivity to tissue influence was investigated by varying the speed of sound and frequency-dependent attenuation. When the restoration results were judged visually, we discovered that the two most critical parameters for two-dimensional (2-D) deconvolution are the lateral focus and the speed of sound. As far as human perception is concerned, we concluded that it is possible to restore *in vivo* RF ultrasound data using an assumed PSF when its error is not significant. However, when the deconvolution results were quantified, we also proved that there are always differences between restored images from various PSFs, which human perception may be insensitive to, but which are identifiable through other metrics such as improvement in the signal-to-noise ratio (ISNR) or correlation. In this article, we will exploit such differences to estimate a PSF parameter which is the speed of sound in this case.

The rest of the article is organised into the following sections. The proposed estimation method for the speed of sound is explained in the Methods section. The applications of the technique to simulations, *in vitro* and *in vivo* measurements are featured in the Results section. Discussions follow on our proposed approach and conclusions are drawn. In Appendix 1, our deconvolution algorithm is introduced.

METHODS

In this section, we describe the methodologies we have employed to estimate the speed of sound. We start with deconvolution and PSF and then discuss a correlation metric capable of choosing the correct speed among numerous deconvolution outputs. Finally, we explain a search strategy to increase the efficiency with which we can select the correct speed.

Deconvolution

The article is mainly concerned with the estimation of the sound speed in medical ultrasound applications. But, the deconvolution of RF ultrasound image data is a pivotal part of our estimation process and is also an important outcome.

When using transducer array probes, the lateral focus is created by a delay profile across the active aperture. But each calculated depth for lateral focus is only valid when the sound speed is known and constant. Such an ideal scenario does not usually occur in real clinical scans, resulting in less than optimal spatial resolution.

Such symptoms have been previously exploited in the estimation of the sound speed (Hayashi et al. 1988; Napolitano et al. 2006), where the delay profiles were repeatedly adjusted until the clearest images were achieved. By using non-blind deconvolution, these symptoms can be explored but with simpler data acquisition. Instead of adjusting the delay pattern for multiple image acquisitions, the non-blind deconvolution enables the use of a single ultrasound scan composed of all beamformed RF data lines. The necessary change is carried out off-line only in the sound speed of a PSF. The comparison of numerous PSFs is conducted through the deconvolution to figure out which PSF best suits the ultrasound data of interest and, hence, produces the clearest restored image. The sound speed used for the best PSF is our estimation of the speed. The metric to determine such best PSF is explained in the Correlation metrics subsection.

Due to its significance in our speed estimation technique, in Appendix 1 we briefly recapitulate the key components of our deconvolution algorithm.

Estimation of the PSF

The main difference between non-blind and blind deconvolution algorithms is whether they need an explicit PSF from the start. In a non-blind algorithm, the explicit PSF can usually be parameterised. This is what makes the estimation of the sound speed feasible through deconvolution.

To estimate the PSF for our non-blind algorithm, we use the Field II simulation program (Jensen 1996). This is an efficient and convenient tool for the type of linear modelling we are engaged in. We calculate the PSF according to what would happen in a largely homogeneous medium: the delay profiles for the transmit and the receive apertures are determined assuming the speed of sound is 1540 m/s, which is normal practice in most diagnostic ultrasound imaging machines. The actual speed of sound in the hypothetical medium can be varied to have any speed. Therefore, when the speed of sound in the simulated medium is made equal or very close to the actual speed in the acquired ultrasound data, the deconvolution will produce the best-possible restoration; as we showed in a previous publication (Shin et al. 2009), a less good PSF produces a less good deconvolution.

Correlation metrics

The overall strategy of our speed estimation method is to run multiple deconvolutions using PSFs with different speeds and to pick the speed which produces the best restoration. Therefore, a metric capable of determining the best outcome is as crucial as the non-blind deconvolution algorithm itself. In a previous article

(Shin et al. 2009), we showed that the deconvolution result could be quantified and demonstrated that the mean correlation length of the restored image is significantly smaller than that of the original ultrasound image, for example, 0.32 and 0.61 mm, respectively (Shin et al. 2009). To this effect, the one-dimensional (1-D) autocorrelation was evaluated along the lateral direction of the images and the half-energy width of the peak was measured.

This correlation length worked well for separating the original ultrasound image from its deconvolved image. However, we found that such a correlation length was not sensitive enough to distinguish deconvolution results with close PSFs from one another (see Fig. 1). A possible explanation for this failure is that most restorations result in physically smaller speckle (see deconvolution images reported by Shin et al. [2009]). The correlation-length approach depends on only a few lags relating to neighbouring pixels and so does not take into account the rest of the longer lags. Therefore, once the speckle (represented by smaller lags in the correlation) was reduced to similar sizes, restorations with similar PSFs may not be easily discriminated through such a correlation metric.

In addressing this challenge, we subsequently discovered that accounting for all the lags in the correlation could be more relevant than the correlation-length metric. The same autocorrelation ($R_{\hat{\mathbf{x}}_i}[l]$) is calculated along the lateral line ($\hat{\mathbf{x}}_i$) at each i-th axial depth of deconvolution image ($\hat{\mathbf{x}}$) as the case for the correlation-length metric and then a summation ($\sum_l |R_{\hat{\mathbf{x}}_i}[l]|$) is made of the magnitude of all the l coefficients of the correlation. To produce a single-valued representation, another summation ($\sum_i \sum_l |R_{\hat{\mathbf{x}}_i}[l]|$)

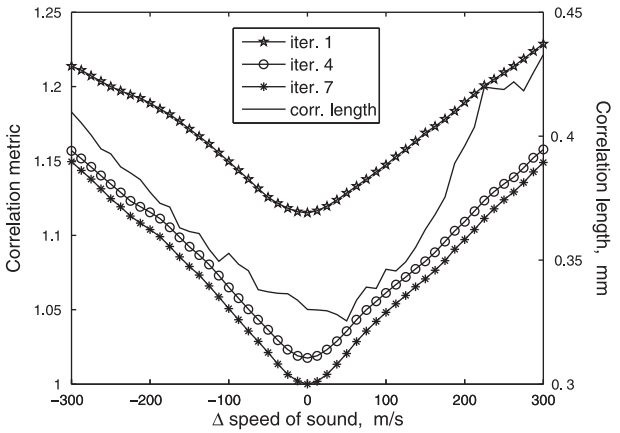

Fig. 1. Plot of correlation metrics vs. various speeds of sound in a simulated phantom for exemplar iteration of deconvolution. The summation-based correlation is normalised by its minimum for display purposes and its scale is shown on the left. The correlation length for the fourth iteration is shown for comparison and its scale is displayed on the right. The spacing between data points is 12.5 m/s and the reference speed ($\Delta = 0$) is 1540 m/s.

was taken of this value for all axial depths. During the course of this article, the correlation metric is evaluated according to this summation-based strategy.

Figure 1 shows a graph of the aforementioned summation-based correlation metric for various speeds of sound in a simulated phantom. The simulation process is explained later in the Simulations subsection within the Results section. The values of the correlation are normalised for display because the metric itself does not directly indicate a meaningful physical quantity but the relative differences are most important. The same convention is followed throughout this article. To produce the data in Figure 1, the PSFs for 49 different speeds were evaluated and the deconvolution algorithm was run for each of them. The speeds of sound in the plot cover the range from –300 to +300 m/s (the reference and correct speed being 1540 m/s) in 12.5 m/s steps denoted by discrete marks. The curves in the graph indicate the correlation metric after different numbers of iterations in the deconvolution algorithm. Increasing the number of iterations is observed to lower the correlation, which indicates an improved restoration. The result illustrates that the correlation metric returns the minimum value when the blurred ultrasound image is deconvolved with the PSF with the correct speed of sound and demonstrates the possibility of finding such a correct value.

Iterative method using non-blind deconvolution

Perhaps, locating the correct speed of sound may be achieved by resorting to a ''brute-force'' approach demonstrated in the Correlation metrics subsection and Figure 1. A method reported by Napolitano et al. (2006) effectively adopts such a strategy. Their core algorithm to determine the correct speed is different from ours but they essentially repeat their algorithm for as many different trial speeds as possible. Although such an approach may be effective, it is not necessarily efficient. Even though the expected range of speeds is widely known for particular types of tissue, the speed in an abnormal tissue may be outside this range. A brute-force approach can also be computationally expensive depending on the resolution between adjacent trial speeds.

The presence of a well-defined distinct minimum in Figure 1 enables us to adopt an optimisation procedure to find the correct speed of sound. We implemented a gradient-descent based approach to track down the optimum speed. As demonstrated in the figure, the local minimum coincides with the global minimum, therefore, we use Newton's method for the optimisation (Press et al. 1992). First, we start with three initial guesses: three different PSFs defined by three different speeds of sound. The flow diagram in Figure 2 illustrates the search process. A single iteration of our deconvolution algorithm (Ng et al. 2007) is carried out with these three PSFs. The

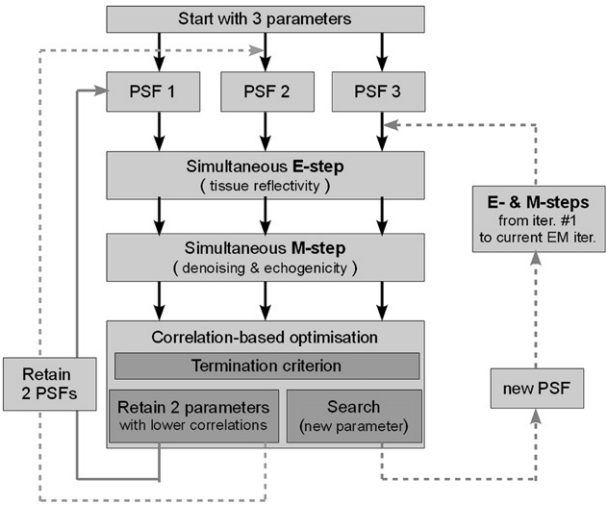

Fig. 2. Flow diagram illustrating the iterative nature of the optimisation searching for the correct speed of sound under an expectation-maximisation (EM) deconvolution framework. The E-step stands for expectation step and M-step for maximisation step. The EM structure is explained in Appendix 1.

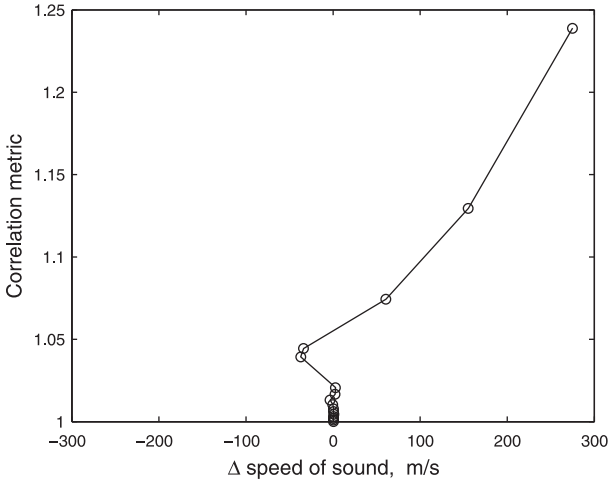

Fig. 3. Exemplar plot showing iterative optimisation process for a simulated phantom and illustrating the eventual convergence. For illustration purposes, a fixed number of 15 iterations were run for this exercise and the last estimated speed was +0.58 m/s away from the exact speed of 1540 m/s. The topmost circular mark indicates the zeroth iteration corresponding to one of the initial guesses.

correlation metrics of the three deconvolutions are calculated and a 1-D quadratic equation is formulated based on the three pairs of sound speeds and corresponding correlation metrics: $f(c) = A\,c^2 + B\,c + C$, where c is the speed of sound, $f(c)$ the correlation metric, and A, B, C coefficients. Then, the next search speed is determined from the first and second derivatives of $f(c)$.

$$c_{i+1} = c_i - \alpha \frac{f'(c_i)}{f''(c_i)} \tag{1}$$

Here, c_{i+1} is the new estimate, c_i the speed having the lowest correlation among three guesses at the i-th iteration of deconvolution and α the step size ($0 < \alpha \leq 1$). Among the three guesses at each iteration, we discard the speed with the highest correlation value, and then move on to the next iteration step of the deconvolution algorithm with three speeds: two being retained from the previous iteration step and the third being the new estimate (c_{i+1}). This procedure is repeated for a fixed number of iterations or until a termination criterion is met. One essential aspect is that the deconvolution stage of the newly-found speed should be updated to the same level as the other two speeds. As shown in Figure 1, the value of the correlation metric is dependent on the number of iterations. And thus, unless the deconvolution status is equal for all three estimates of the speed, the quadratic equation will not represent the true trend of the optimisation process. This update routine makes the algorithm slower in each successive iteration. An example of computational cost can be found in the Discussions section.

Figure 3 shows an exemplar outcome of the optimisation scheme adopted in our algorithm. The data shown in the figure are obtained from the same simulation used in Figure 1. Each circular mark denotes the sound speed and the corresponding correlation metric of the estimation at each deconvolution stage. Rapid convergence on the optimal speed is observed. Table 1 is a numerical counterpart of Figure 3. The standard deviation in the table is taken for the three speed guesses at each deconvolution stage and is shown to drop quickly as the optimisation process converges. This illustrates that the standard deviation can be used as a termination criterion of the algorithm. For example, if the standard deviation of 0.10% based on the estimated speed is deemed sufficiently small, this particular exercise could have been terminated as early as the ninth iteration.

RESULTS

In this section, we present the results of our speed-estimation algorithm applied to simulations, *in vitro* and *in vivo* measurements. All the results in this section are obtained from RF 2-D ultrasound image data.

Simulations

First, we applied our sound-speed estimation technique to a 2-D simulated phantom. The way the simulation was conducted is explained in this subsection.

A 2-D imaginary phantom was created with five circles whose geometry is shown in Figure 4. This five-circle configuration corresponds to an echogenicity map characterised by macroscopically smooth features. The reflectivity within each scatterer type is then randomised

Table 1. Iteration statistics of the algorithm, equivalent to the data in Figure 3.

Iteration	Speed estimate (m/s)	Standard deviation (m/s)	Standard deviation (%)
0	+275.000	25.000	1.377
1	+155.370	63.102	3.722
2	+60.740	94.630	5.912
3	−33.890	94.630	6.283
4	−37.159	55.602	3.700
5	+2.800	22.187	1.438
6	+2.339	21.051	1.365
7	−3.372	3.438	0.224
8	−0.209	1.620	0.105
9	+0.527	1.311	0.085
10	+0.445	0.403	0.026
11	+0.956	0.274	0.018
12	+0.663	0.110	0.007
13	+0.539	0.051	0.003
14	+0.511	0.014	0.001
15	+0.579	0.027	0.002

The second column shows the difference of the new estimate from the reference speed of 1540 m/s. The standard deviation is taken for three speeds used at each iteration of the optimisation process. Two of the three speeds are not shown in the table. The zeroth iteration corresponds to the initial guesses.

by incorporating a Gaussian distribution which represents microscopic fluctuations. A reference image for the reflectivity function is displayed in Figure 4a. The bright circles are 10 times stronger than the background scatterers, the dark ones are 10 times weaker, and the medium one is three times stronger.

We blur the reflectivity function by calculating a forward convolution of the RF image data in Figure 4a with the PSF evaluated by Field II. The speed of sound was chosen as 1540 m/s. After blurring, zero-mean white Gaussian noise is added to the simulated ultrasound image, which is illustrated in Figure 4b. The signal-to-noise ratio after the addition of the noise is 40 dB. The ultrasound data was demodulated to baseband, envelope detected and logarithmically compressed into 60 dB dynamic range. When interpreting the image in Figure 4b, it is useful to note that the axial depth of the lateral focus corresponds to the designed centre of the middle circle. More serious blurring is easily spotted for scatterers away from the axial depth of the lateral focus. One can also notice the presence of coarse speckle in Figure 4b.

The blurred and noisy image in Figure 4b is restored using the algorithm by Ng et al. (2006, 2007), whose core structure is outlined in Appendix 1. At any given iteration of deconvolution, we have three PSFs with different speeds of sound and the deconvolution algorithm is run concurrently for these three estimations as described in the Methods section. Graphs showing correlation metrics and the convergence pattern have already been introduced in Figures 1 and 3.

An example result of the deconvolution is shown in Figure 4c. The restored image is the outcome of our speed estimation process. The estimated sound speed is +0.53 m/s away from the correct speed of 1540 m/s, when the optimisation process is terminated at the ninth iteration of deconvolution (see Table 1, using the standard deviation of 0.10% and lower). A high degree of restoration is observed. The once blurred circles appear once again circular with sharp boundaries. Furthermore, the speckle size is significantly reduced, but the speckle is retained, which is important because this textural information can be usefully interpreted in clinical applications.

One may ask why the deconvolved result does not look perceptually the same as the designed reflectivity function despite the use of almost the same PSF for both forward and backward operations in the simulation. This is because of the presence of the additive Gaussian noise and because of the blurring which involves some loss of high frequency information and consequently causes the deblurring problem to be ill-posed.

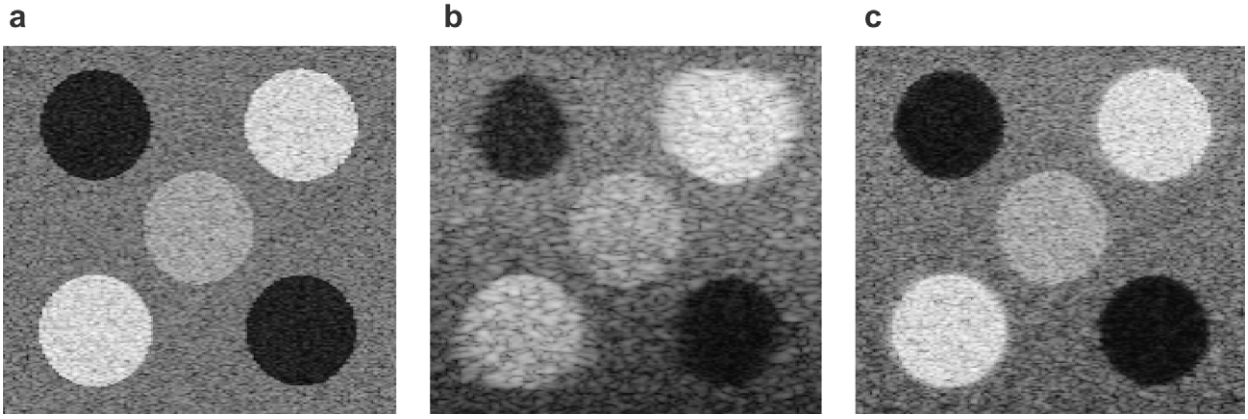

Fig. 4. Images for the simulation: (a) reflectivity function, (b) blurred image with additive white Gaussian noise of SNR = 40 dB and (c) deconvolution by the optimum speed (Δ = +0.53 m/s). The dynamic range of the logarithmically compressed images is 60 dB.

In vitro measurements on a phantom with a known speed of sound

After verifying the operation of our sound-speed estimation technique in the simulation, we proceeded to apply the estimation algorithm to *in vitro* data sets. First, we applied our speed-of-sound estimation method to an *in vitro* phantom with a known speed of sound. The phantom has several spheres with back-scattering strengths different from the background. It was manufactured by the Ultrasound Research Group at the University of Wisconsin-Madison. The sound speed of the phantom is around 1545 m/s, which is based on the speed measurements of its components conducted by the manufacturer. Due to some level of diffusion between adjacent components, there could be uncertainty of approximately ±5 m/s in its average speed of sound. In addition, no information is available on the temperature dependence of its sound speed. Therefore, some error in our estimation method could be caused by these uncertainties. Nonetheless, we treat the speed of 1545 m/s as the ground truth for this phantom.

Throughout this article, the following ultrasound system was used to acquire the RF data for *in vitro* and *in vivo* measurements. The system consisted of a General Electric probe RSP6-12 (GE Healthcare, Chalfont St Giles, Buck, UK) and a Diasus ultrasound machine from Dynamic Imaging Ltd. (Dynamic Imaging used to be based near Edinburgh in Scotland, but they are no longer in business), which was synchronised with a Gage Compuscope CS14200 digitiser (Gage Applied Technologies, Lockport, IL, USA). The digitisation process was linked to the locally-developed Stradwin software, which is a user-friendly cross-platform tool for medical ultrasound acquisition and visualisation, based on Stradx system (Prager et al. 1999).

The GE probe is composed of a linear transducer array with 192 piezoelectric elements. The pitch between the centres of adjacent elements is 0.197 mm. Its centre frequency was measured to be 8 MHz. The estimated radius of the elevational focus is 9.6 mm. As the Diasus system has 128 A-line capability, the middle 128 elements of the GE probe were connected to the Diasus system. The beamforming of the Diasus machine operates an active aperture of 32 elements with fixed-depth transmit and receive foci. It uses time-gain compensation and logarithmic compression for display on its built-in monitor. However, uncompressed RF data after beamforming are digitised at the sampling rate of 66.67 MHz with a resolution of 14 bits.

Figure 5 shows a result of the algorithm applied to the known-speed phantom. The speed estimation of the last (15th) iteration is +1.50 m/s away from the speed of 1545 m/s. The smooth dashed curve in the graph is obtained by running the deconvolution algorithm concurrently for

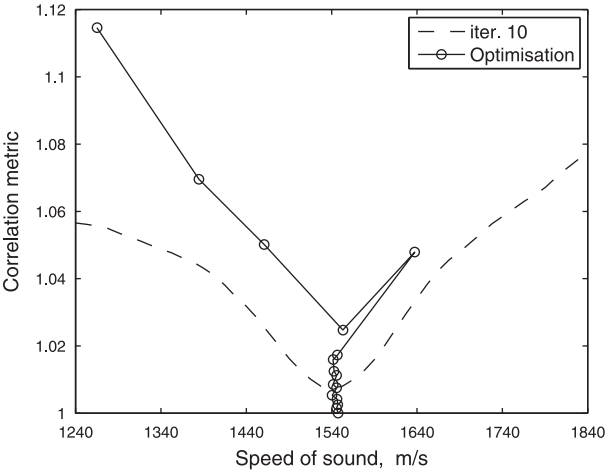

Fig. 5. Exemplar plot showing iterative optimisation process for an *in vitro* phantom with a known sound speed of 1545 m/s. The topmost circular mark indicates the zeroth iteration corresponding to one of the initial guesses. The smooth curve was obtained by running the deconvolution algorithm with PSFs having 49 different speeds at the 10th iteration.

49 different speeds of sound as shown in Figure 1. This process of parallel running is not required for our speed optimisation procedure but is shown additionally to demonstrate that our optimisation step does converge to the minimum for an *in vitro* measurement as well. We have also conducted estimations for further data sets having different lateral focus settings. The overall estimation error for this phantom turned out to be –6.82 ± 4.82 m/s (or –0.44 ± 0.31%) in a notation of ''mean ± standard deviation''.

In vitro measurements on phantoms with unknown speeds of sound

Now we turn our attention to *in vitro* phantoms with speeds of sound that are not known *a priori*. We locally produced ultrasound tissue-mimicking phantoms by mixing agar powder, scatterers and water (Burlew et al. 1980). The speed of sound is not known for these in-house phantoms *a priori* and, hence, we measured it independently of our deconvolution-based estimation method. We applied a time-of-flight method by measuring the time for sound to travel between known positions. Wires were put inside phantoms to determine travelling distances. The time-of-flight method was chosen over other existing techniques because the same ultrasound data can be used for it and our deconvolution-based method.

For the time-of-flight technique, we chose an A-line with the least blurring of the target wires. Then, its envelope was detected with the Hilbert transform and the peaks from the wires were selected as known reference locations. The distance (10 mm) between wires was taken from their geometric design but was not actually measured. The travelling time was then worked out

from the number of samples between wire peaks and the sampling rate of 66.67 MHz. Hence, the speed of sound between the wires is easily estimated.

We have repeated the same set of exercises for the in-house phantoms as for the simulation and the known-speed phantom: finding the correct average speed *via* the deconvolution-based optimisation and running multi-speed deconvolution for comparison purpose. Figure 6 shows an exemplar result obtained from an *in vitro* in-house phantom measurement. One interesting aspect of the optimisation curve is that there is a peculiar overshoot in the fourth iteration. That is because the pairs of speed guesses and corresponding correlation metrics at this iteration do not conform to our quadratic assumption but rather to a linear formulation having a very small $f''(c_i)$ in eqn (1). However, the algorithm is robust enough to correct such odd behaviour. In the figure, we also show an independent measurement of the sound speed by the time-of-flight method (the vertical dotted line). The speed estimations for this example are 1455.89 m/s by the deconvolution and 1460.46 m/s by the time-of-flight method.

More RF ultrasound data sets were acquired for *in vitro* in-house phantoms with various lateral focal depths and different wire alignments. The graphic information is shown in Figure 7 illustrating the estimation errors of our algorithm when the time-of-flight estimations are taken as the ground truth. The overall estimation error is +0.01 ± 0.60 % (+0.19 ± 8.90 m/s). Anderson and Trahey (1998) quoted errors of –0.05 % (–0.67 m/s) ± 0.44% and –0.18 % (–2.77 m/s) ± 0.52% for phantoms composed

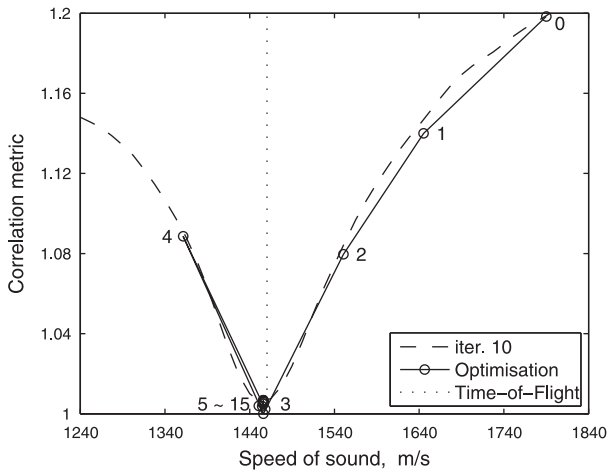

Fig. 6. Exemplar plot showing the iterative optimisation process for an *in vitro* in-house phantom with an unknown speed of sound. Integers next to circles indicate the iteration numbers and the zeroth iteration corresponds to one of the initial guesses. The correlation metric obtained at the 10th iteration of deconvolution with 49 PSFs is also shown in the smooth dashed curve. The speed was also independently measured by the time-of-flight method denoted by the vertical dotted line, in which the y-axis value is irrelevant.

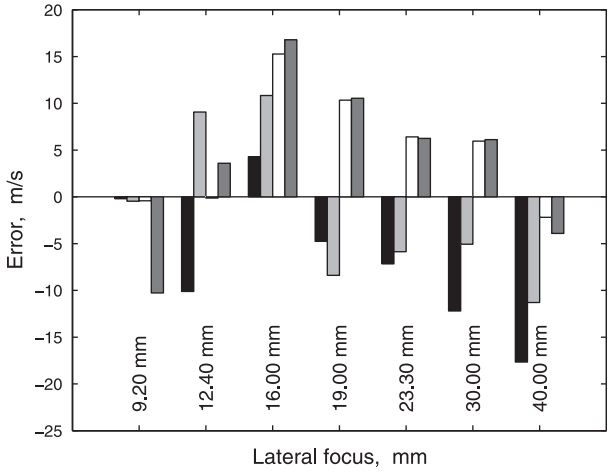

Fig. 7. The error associated with the sound-speed estimation for *in vitro* in-house phantoms using deconvolution. The reference speeds were those measured by the time-of-flight method. The four different levels of grey at each lateral focal depth indicate different wire alignments: parallel or perpendicular (and mixture of the two) to the B-mode image. The delay profile for the lateral focus was set assuming a sound speed of 1540 m/s.

of sponge and agar-graphite, respectively (see Table 1 in their publication).

Previously (Shin et al. 2009), we analysed the sensitivity of the ultrasound deconvolution to the parameters of the PSF. The speed of sound is one of the parameters investigated in the study. It was discovered that restored images by two different PSFs would be judged differently in human perception when their parameters were significantly different. The finding served as one of the motivations in this article: we may be able to produce a restored image better than that deconvolved by the PSF having the assumed speed of 1540 m/s, when the original ultrasound image was acquired from tissue having sound speed far away from 1540 m/s. So far, we have demonstrated that our algorithm is capable of estimating the speed of sound in tissue-mimicking materials. Now, in Figure 8, we provide the evidence of a further enhanced image by restoration with an optimum speed of sound. The image (a) is the original ultrasound image acquired by an ultrasound system whose beamforming delay is set to the sound speed of 1540 m/s. The image (b) is the restoration by an optimum speed of sound (1455.89 m/s) estimated by our algorithm. The image (c) is the restored image by the PSF having the speed of 1540 m/s. It is clear that the deconvolution result *via* 1540 m/s has smaller speckle sizes and smaller footprint of a wire at the centre than those of the original image. However, it is observed that the deconvolution image by an optimum speed of sound has the best quality: the wire at the centre is restored to its original circular shape and speckle in the surrounding area is clearly smaller than that from both the original ultrasound image and the deconvolution by a nominal

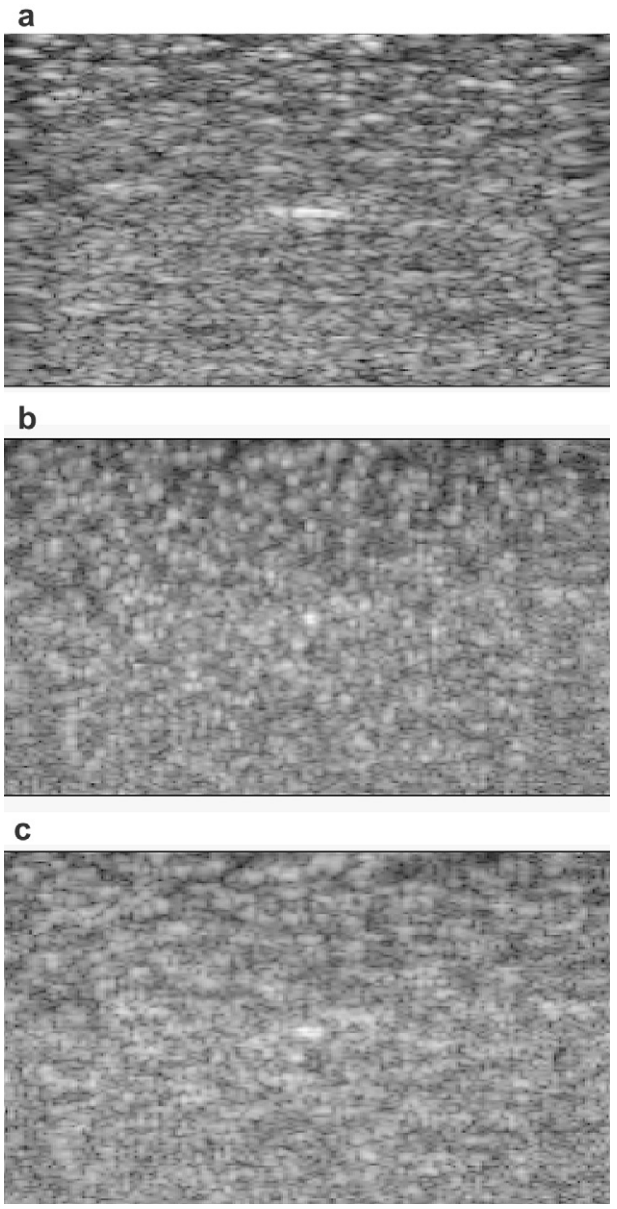

Fig. 8. Ultrasound images of an *in vitro* in-house phantom: (a) original ultrasound image, (b) deconvolution by an optimum speed of 1455.89 m/s and (c) deconvolution by a nominal speed of 1540 m/s. The size of the images is 14.6 mm × 25.0 mm, when the speed of sound is assumed to be 1540 m/s for comparison purposes. The ultrasound data set is the same as that used in Figure 6. The dynamic range of the logarithmically compressed images is 60 dB. The wire is in the centre of each image. Note its size changes at each image.

speed of 1540 m/s. It is also noted that the presence of the wire in the image is not likely to influence the sound speed estimated in the phantom due to its small size.

In vivo measurements

We have also run our algorithm on two *in vivo* ultrasound data sets taken freehand from human subjects. The experimental protocol was reviewed by a local ethics committee and informed consent of the subjects was obtained. The first example is a testicle. The result showing the convergence of the algorithm is displayed in Figure 9. Our optimisation algorithm converges to the minimum and the estimated speed of sound is 1521.37 m/s. The ultrasound images are illustrated in Figure 10. Unlike the stark perceptual difference noticed in the *in vitro* phantom of Figure 8, the two restoration images from Figure 10b (using 1521.37 m/s) and Figure 10c (using 1540 m/s) appear very similar. However, it is clear that both deconvolution solutions are enhanced greatly from the original ultrasound B-scan in Figure 10a. The speckle size is reduced and the image resolution is finer through the deblurring effect of the deconvolution.

The minimal perceptual dissimilarity may be attributed to the fact that the difference of the speeds used for both deconvolutions is not very large. For example, the speed difference in the *in vitro* case in Figure 8 is 84.11 m/s. In contrast, the difference for this *in vivo* example is 18.63 m/s. Such perceptual insensitivity in Figure 10 due to a small speed difference was also one of the findings in our previous publication (Shin et al. 2009).

The second example is a forearm. Figures 11 and 12 illustrate the convergence of the estimation algorithm and the ultrasound images, respectively. The estimated sound speed is 1571.74 m/s, which is in the expected range for muscle: 1542∼1626 m/s (see Table 1-1 in Angelsen 2000). Compared with the original B-scan in Figure 12a, the lateral (horizontal) correlation and the speckle size in the areas of diffuse scattering are both reduced in deconvolution images in Figure 12b and c. There is, however, axial (vertical) ghosting in regions of

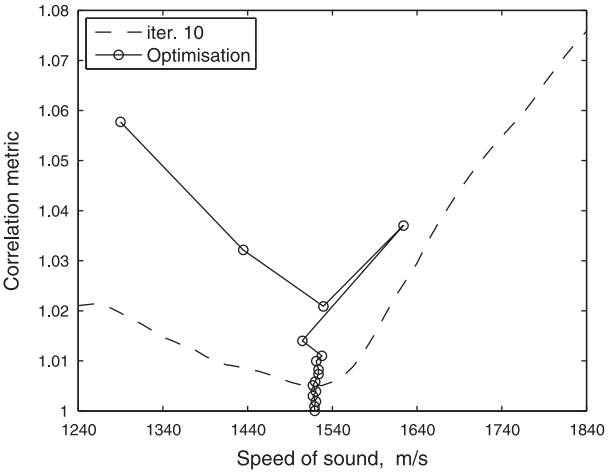

Fig. 9. Exemplar plot showing the iterative optimisation process for an *in vivo* scan of a human testicle. The topmost circular mark indicates the zeroth iteration corresponding to one of the initial guesses. The correlation metric obtained at the 10th iteration of deconvolution with 49 PSFs is also shown in the smooth dashed curve.

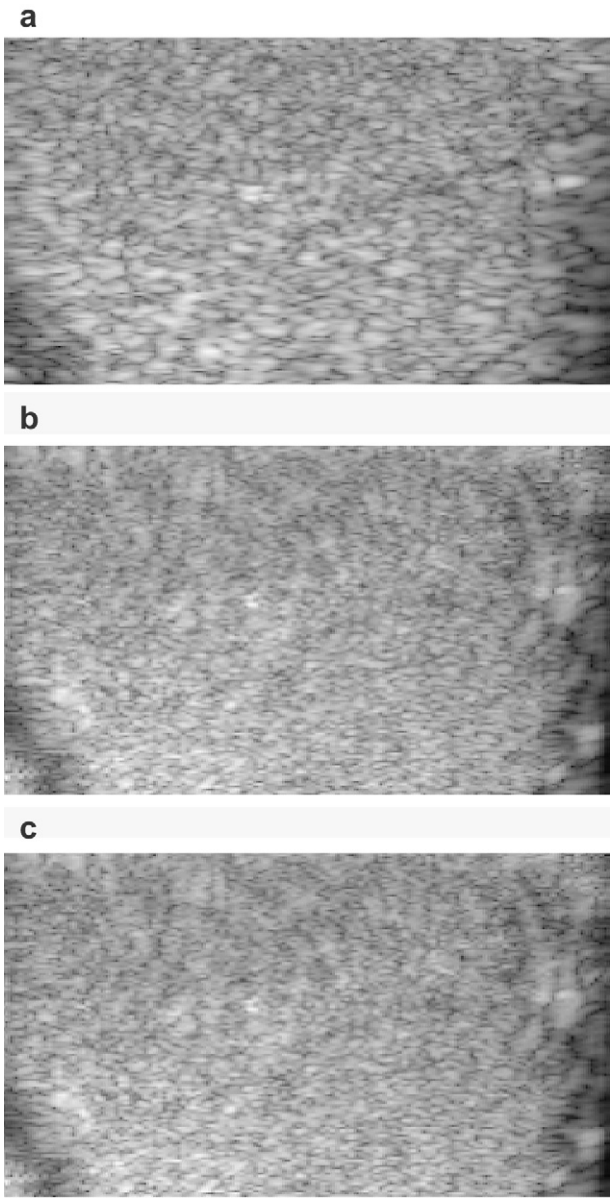

Fig. 10. Ultrasound images of an *in vivo* human testicle: (a) original ultrasound image, (b) deconvolution by an optimum speed of 1521.37 m/s and (c) deconvolution by a nominal speed of 1540 m/s. The size of the images is 14.6 mm × 25.0 mm, when the speed of sound is assumed to be 1540 m/s for comparison purposes. The ultrasound data set is the same as that used in Figure 9. The dynamic range of the logarithmically compressed images is 60 dB.

specular reflection that degrades the clarity of the image. This artefact is attributed to an approximation in this and many other deconvolution algorithms, in which the ultrasound image formation is modelled as a result of weak diffuse scattering (Abeyratne et al. 1995; Adam and Michailovich 2002; Husby et al. 2001; Jensen 1992; Michailovich and Adam 2004; Taxt 2001; Taxt and Strand 2001; Wan et al. 2003).

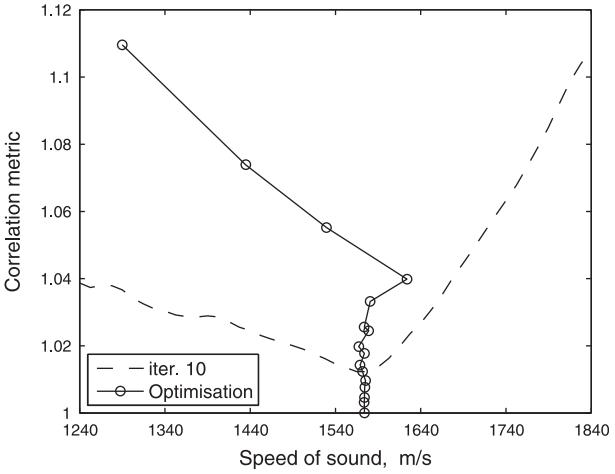

Fig. 11. Exemplar plot showing the iterative optimisation process for an *in vivo* scan of a human forearm. The topmost circular mark indicates the zeroth iteration corresponding to one of the initial guesses. The correlation metric obtained at the 10th iteration of deconvolution with 49 PSFs is also shown in the smooth dashed curve.

This ghosting effect is often worse when the deconvolution algorithm runs for more iterations. Therefore, when specular reflection is present, a less degraded restoration image can be obtained by using fewer iterations. Images (b) and (c) in Figure 12 were produced using two iterations while the estimated speed for image (b) was obtained by allowing the algorithm to run to convergence. The previous restored images in Figures 8b and 10b do not contain significant specular reflections, so in these cases the deconvolution algorithm was run to convergence. For comparison purposes, the corresponding images in Figures 8c and 10c were produced with the same numbers of iterations as in Figures 8b and 10b, respectively.

DISCUSSION

Although our proposed technique for medical ultrasound speed estimation has several advantages over other methods reported in previous publications, there are still limitations and room for further improvement in the approach. Perhaps, the greatest shortcoming of all is its inability to handle inhomogeneous tissues. Currently, our algorithm is not equipped to directly deal with the correction of phase aberration, which is often created by irregular layers through which ultrasound travels. There is a potential risk of estimating the speed incorrectly especially *in vivo*, where the received RF signals usually have to pass through the human skin interface whose speed may be different from the rest of the tissue. Because the PSF we use in this article assumes homogeneity, our correlation

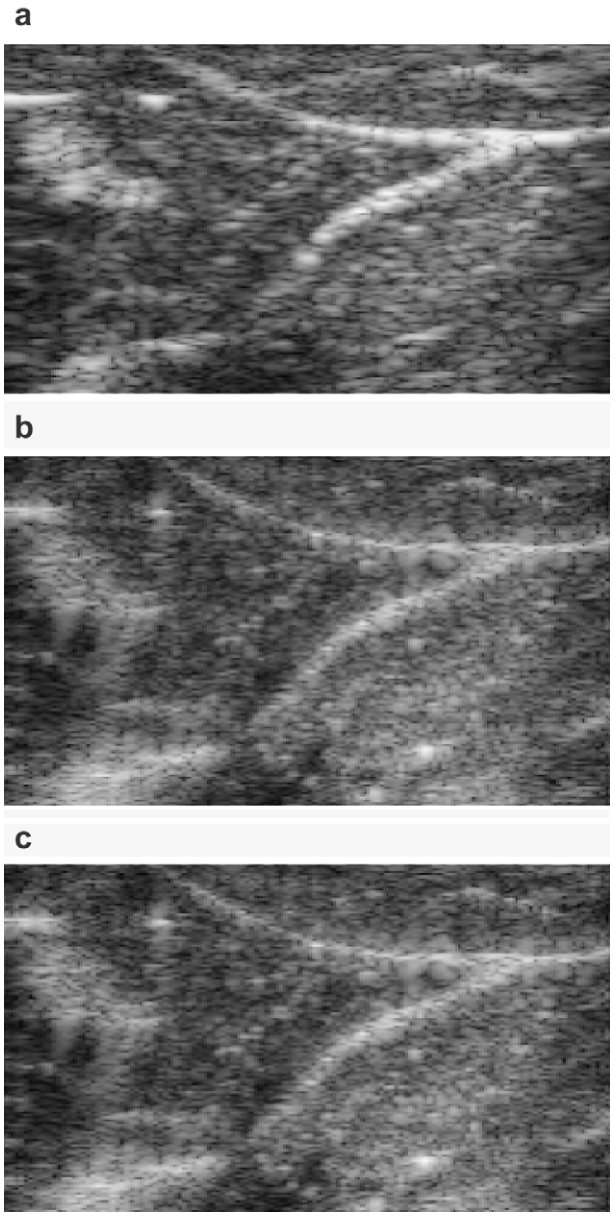

Fig. 12. Ultrasound images of an *in vivo* human forearm: (a) original ultrasound image, (b) deconvolution by an optimum speed of 1571.74 m/s and (c) deconvolution by a nominal speed of 1540 m/s. The size of the images is 14.6 mm × 25.0 mm, when the speed of sound is assumed to be 1540 m/s for comparison purposes. The ultrasound data set is the same as that used in Figure 11. The dynamic range of the logarithmically compressed images is 60 dB.

metric is likely to select a weighted mean value among different speeds of sound.

The fact that the deconvolved image (for example in Fig. 10) is significantly improved from the original B-mode image may suggest that the PSF used for the restoration is close to the exact but unknown PSF inherent in the acquired ultrasound data. This is because, in our previous findings (Shin et al. 2009), we showed that the image restoration could turn out degraded if the assumed PSF is far away from the true one.

In tissue with non-uniform sound speed, the algorithm may produce a result that is other than a weighted mean of the constituent speeds. When correlation metrics are plotted at different speeds, there may be several local minima, or a plateau of minima rather than a dominant minimum. In these scenarios, our particular use of an optimisation-based solution may have adverse implications because it pursues a local minimum that is usually the nearest to the set of initial guesses. To reduce this risk, the algorithm may be run again with a completely different set of initial speeds. Alternatively, a parallel run of deconvolution with a small number of PSFs based on different sound speeds may be used to indicate such undesirable behaviour.

Another potential obstacle to clinical application could be the computational expense compared with other published methods of speed estimation. In our previous publication (Shin et al. 2009), we reported maximum computing costs of 160 s for a PSF and 50 s for deconvolution based on two iterations. The figures were measured for an image size of 256 × 128 using Matlab on a 32 bit Windows XP platform at 2.40 GHz clock speed. Based on these values, our proposed method may take approximately $160\,(n-1) + 25\,(2\,n + \sum_{i=1}^{n} i)$ s for n iterations when three PSFs for the first iteration are precomputed. For an early termination ($n = 9$) in Figure 4c, which is based on the image size of 256 × 128, it takes about 2855 (= 1280 + 1575) s including both parts of PSFs and deconvolution. If we use precomputed PSFs based on ''rounded'' speeds of sound, it could take less than 27 min.

To estimate the speed of sound accurately and reliably, the other parameters required to build a PSF must be correct as well. For the list of parameters, see the penultimate paragraph of the Introduction and Literature section. We showed that those parameters could be assigned to certain families according to their characteristics (Shin et al. 2009). For example, the speed of sound exhibited a similar pattern of behaviour as the lateral focus did for 2-D images, and the elevational focus was in the same group as the element height. Therefore, the accuracy of the sound-speed estimation is most likely to be affected by that of the lateral focus. In our framework, what matters for the lateral focus is not how the focus is realised through soft tissues but the intended delay profile applied to the imaging machine, which is not disturbed by the tissue. Because we know the delay profiles that were used, it is unlikely that our estimation of the sound speed is susceptible to uncertainty in the lateral focus.

In future work, the development of a technique designed for multilayered or heterogeneous soft tissue

would undoubtedly increase further the clinical value of our deconvolution-based estimation method. The core challenge would be the creation of a PSF model that reflects the inhomogeneous nature of soft tissue encountered clinically. In doing so, we will start with a simplest possible case and gradually consider more complex cases. The axial speed variation might be addressed by implementing layered media while the lateral variation of speed might be characterised by using a subset of the A-lines or by simple translation of the probe.

CONCLUSIONS

We have constructed an iterative algorithm using non-blind ultrasound data deconvolution capable of estimating the average speed of ultrasound in homogeneous tissues. The use of deconvolution enables our technique to have simple data acquisition requirements compared to other reported methods. No special equipment is required for the speed estimation process and the data can be collected freehand through traditional use of a single transducer array in the ultrasound imaging system.

Our estimation approach has been validated in simulations, *in vitro* phantoms with various speeds of sound, and *in vivo* scans. Its estimation error for *in vitro* in-house phantoms, for example, was measured to be $+0.19 \pm 8.90$ m/s ($+0.01 \pm 0.60\%$) in mean $\pm$ standard deviation, based on the speeds measured independently by the time-of-flight method.

In addition to the speed estimation itself, our method has also proved to be capable of simultaneously producing a better restoration of the ultrasound image data than deconvolution by an assumed speed of 1540 m/s, when this assumption is incorrect.

Acknowledgements—The work was funded by the Engineering and Physical Sciences Research Council (reference EP/E007112/1) in the United Kingdom.

REFERENCES

Abeyratne UR, Petropulu AP, Reid JM. Higher order spectra based deconvolution of ultrasound images. IEEE Trans Ultrason Ferroelectr Freq Control 1995;42:1064–1075.

Adam D, Michailovich O. Blind deconvolution of ultrasound sequences using nonparametric local polynomial estimates of the pulse. IEEE Trans Biomed Eng 2002;49:118–131.

Anderson ME, McKeag MS, Trahey GE. The impact of sound speed errors on medical ultrasound imaging. J Acoust Soc Am 2000;107: 3540–3548.

Anderson ME, Trahey GE. The direct estimation of sound speed using pulse-echo ultrasound. J Acoust Soc Am 1998;104:3099–3106.

Angelsen BAJ. Ultrasound imaging: Waves, signals, and signal processing, Vol I. Trondheim, Norway: Emantec AS; 2000.

Burlew MM, Madsen EL, Zagzebski JA, Banjavic RA, Sum SW. A new ultrasound tissue-equivalent material. Radiat Phys 1980;134: 517–520.

Flax SW, O'Donnell M. Phase-aberration correction using signals from point reflectors and diffuse scatterers: Basic principles. IEEE Trans Ultrason Ferroelectr Freq Control 1988;35:758–767.

Hayashi N, Tamaki N, Senda M, Yamamoto K, Yonekura Y, Torizuka K, Ogawa T, Umemura KKC, Kodama M. A new method of measuring *in vivo* sound speed in the reflection mode. J Clin Ultrasound 1988; 16:87–93.

Husby O, Lie T, Langø T, Hokland J, Rue H. Bayesian 2-D deconvolution: A model for diffuse ultrasound scattering. IEEE Trans Ultrason Ferroelectr Freq Control 2001;48:121–130.

Jellins J, Kossoff G. Velocity compensation in water-coupled breast echography. Ultrasonics 1973;11:223–226.

Jensen J. Field: A program for simulating ultrasound systems. Med Biol Eng Comput 1996;34:351–353.

Jensen JA. Deconvolution of ultrasound images. Ultrason Imaging 1992; 14:1–15.

Kingsbury N. Image processing with complex wavelets. Philos Trans R Soc Lond A 1999;357:2543–2560.

Kingsbury N. Complex wavelets for shift invariant analysis and filtering of signals. Appl Comput Harmon Anal 2001;10:234–253.

Kondo M, Takamizawa K, Hirama M, Okazaki K, Iinuma K, Takehara Y. An evaluation of an *in vivo* local sound-speed estimation technique by the crossed beam method. Ultrasound Med Biol 1990; 16:65–72.

Krücker JF, Fowlkes JB, Carson PL. Sound-speed estimation using automatic ultrasound image registration. IEEE Trans Ultrason Ferroelectr Freq Control 2004;51:1095–1106.

Michailovich O, Adam D. Phase unwrapping for 2-D blind deconvolution of ultrasound images. IEEE Trans Med Imaging 2004;23: 7–25.

Napolitano D, Chou CH, McLaughlin G, Ji TL, Mo L, DeBusschere D, Steins R. Sound- speed correction in ultrasound imaging. Ultrasonics 2006;44:e43–e46.

Ng GC, Freiburger PD, Walker WF, Trahey GE. A speckle target adaptive imaging technique in the presence of distributed aberrations. IEEE Trans Ultrason Ferroelectr Freq Control 1997;44:140–151.

Ng GC, Worrell SS, Freiburger PD, Trahey GE. A comparative evaluation of several algorithms for phase aberration correction. IEEE Trans Ultrason Ferroelectr Freq Control 1994;41:631–643.

Ng J, Prager R, Kingsbury N, Treece G, Gee A. Modeling ultrasound imaging as a linear shift-variant system. IEEE Trans Ultrason Ferroelectr Freq Control 2006;53:549–563.

Ng J, Prager R, Kingsbury N, Treece G, Gee A. Wavelet restoration of medical pulse-echo ultrasound images in an EM framework. IEEE Trans Ultrason Ferroelectr Freq Control 2007;54:550–568.

Nock L, Trahey GE, Smith SW. Phase aberration correction in medical ultrasound using speckle brightness as a quality factor. J Acoust Soc Am 1989;85:1819–1833.

Ophir J, Yazdi Y. A transaxial compression technique (TACT) for localized pulse-echo estimation of sound speed in biological tissues. Ultrason Imaging 1990;12:35–46.

Pereira FR, Machado JC, Pereira WCA. Ultrasonic wave speed measurement using the time-delay profile of rf-backscattered signals: Simulation and experimental results. J Acoust Soc Am 2002;111:1445–1453.

Prager R, Gee A, Berman L. Stradx: Real-time acquisition and visualization of freehand three-dimensional ultrasound. Med Image Anal 1999;3:129–140.

Press WH, Teukolsky SA, Vetterling WT, Flannery BP. Numerical recipes in C, The art of scientific computing. 2nd edition. Chapter 10. Minimization or maximization of functions. Cambridge, UK: Cambridge University Press; 1992.

Robinson DE, Ophir J, Wilson LS, Chen CF. Pulse-echo ultrasound speed measurements: progress and prospects. Ultrasound Med Biol 1991;17:633–646.

Sendur L, Selesnick IW. Bivariate shrinkage functions for wavelet-based denoising exploiting interscale dependency. IEEE Trans Signal Process 2002;50:2744–2756.

Shin HC, Prager R, Ng J, Gomersall H, Kingsbury N, Treece G, Gee A. Sensitivity to point-spread function parameters in medical ultrasound image deconvolution. Ultrasonics 2009;49:344–357.

Taxt T. Three-dimensional blind deconvolution of ultrasound images. IEEE Trans Ultrason Ferroelectr Freq Control 2001;48:867–871.

Taxt T, Strand J. Two-dimensional noise-robust blind deconvolution of ultrasound images. IEEE Trans Ultrason Ferroelectr Freq Control 2001;48:861–866.

Therrien CW. Discrete random signals and statistical signal processing. Englewood Cliffs, NJ: Prentice Hall, Inc; 1992.

Wan S, Raju BI, Srinivasan MA. Robust deconvolution of high-frequency ultrasound images using higher-order spectral analysis and wavelets. IEEE Trans Ultrason Ferroelectr Freq Control 2003; 50:1286–1295.

APPENDIX 1

DECONVOLUTION ALGORITHM

Because of its importance in our approach, we briefly introduce the key components of our deconvolution algorithm for the benefit of readers who may not be familiar with it. Here, we present the algorithm with the minimum use of mathematics, and introduce simple numeric examples to help understanding of the basics. As a graphical guide, the core structure is illustrated in Figure 13. Complete details can be found in previous publications (Ng et al. 2006, 2007).

In our ultrasound image formation model, the wave propagation is assumed linear. Although nonlinearity is present in *in vivo* scans of clinical applications, our approach is still applicable to ultrasound images when dominated by linearity. In medical ultrasound imaging, linearity is generally preserved in pulse propagation and reflection, with higher order harmonic imaging as exceptions (Taxt 2001). Without loss of generality, the ultrasound image formation can be mathematically modelled as follows with a variable $\mathbf{x}$ as the reflectivity function, which is our goal to compute, and $\mathbf{y}$ as the measured ultrasound signal, which is blurred and noisy in nature.

$$\mathbf{y} = \mathbf{H}\,\mathbf{x} + \mathbf{n} \tag{2}$$

Potential measurement errors are taken into account as additive white Gaussian noise ($\mathbf{n}$). $\mathbf{H}$ is a block diagonal matrix along the lateral dimension that represents the blurring of the reflectivity function during the imaging process. Each block matrix maps from the axial depth dimension to the time domain at a given lateral position. Here, two–dimensional data ($\mathbf{y}$, $\mathbf{x}$, $\mathbf{n}$) are rearranged into one-dimensional equivalents by lexicographic ordering and, thus, the sizes of the vectors and the matrix are: $N \times 1$ for $\mathbf{x}$, $\mathbf{n}$, and $\mathbf{y}$, and $N \times N$ for $\mathbf{H}$. Here, N is the total image size.

Our goal in deconvolution is to estimate the reflectivity function $\mathbf{x}$ from blurred and noisy RF ultrasound data $\mathbf{y}$. Perhaps, we can imagine a simple numerical example of eqn (2) to help understanding: $\begin{bmatrix}-2.1\\-0.9\end{bmatrix}=\begin{bmatrix}6&2\\3&1\end{bmatrix}\begin{bmatrix}-1\\2\end{bmatrix}+\begin{bmatrix}-0.1\\0.1\end{bmatrix}$. Here, we aim to determine $\mathbf{x}\begin{pmatrix}-1\\2\end{pmatrix}$, when we have ultrasound data $\mathbf{y}\begin{pmatrix}-2.1\\-0.9\end{pmatrix}$. It is clear that the characteristics of $\mathbf{x}$ and $\mathbf{y}$ are very different, as is usual in an ultrasound imaging situation. We can also see that individual elements of $\mathbf{y}$ are influenced by all elements in $\mathbf{x}$ instead of corresponding to single elements of $\mathbf{x}$. This combined influence or interference is known as ''convolution'' in mathematics; and, hence, reversing the process to get $\mathbf{x}$ from $\mathbf{y}$ is ''deconvolution''. The easiest attempt at deconvolution may be a simple inversion: $\mathbf{x} = \mathbf{H}^{-1}(\mathbf{y} - \mathbf{n})$. Unfortunately, there are two obstacles for this: the PSF $\mathbf{H}\begin{pmatrix}6&2\\3&1\end{pmatrix}$ in this example is not invertible, and in general it is not possible to know the noise $\mathbf{n}\begin{pmatrix}-0.1\\0.1\end{pmatrix}$ exactly. However in non-blind deconvolution the PSF is known *a priori* (as in the scenarios discussed in this article). Therefore, instead of finding the exact $\mathbf{x}$, we aim to evaluate an estimate $\hat{\mathbf{x}}$ after imposing extra restrictions or including prior information about $\mathbf{x}$, which may be seen as reducing the number of potential candidates for $\hat{\mathbf{x}}$. Since the exact $\mathbf{n}$ cannot be determined, we also assume prior information about it. This technique for including prior knowledge is known as the Bayesian approach in statistics.

There are many ways of assigning priors on $\mathbf{x}$ and $\mathbf{n}$ but the most popular choice is to assume that both $\mathbf{x}$ and $\mathbf{n}$ follow Gaussian distributions, which is valid practice in many circumstances. Then, a solution to the deconvolution problem of estimating $\hat{\mathbf{x}}$ becomes the well-known Wiener filter. With a further assumption, the Wiener filter is simplified to give zero-order Tikhonov regularisation.

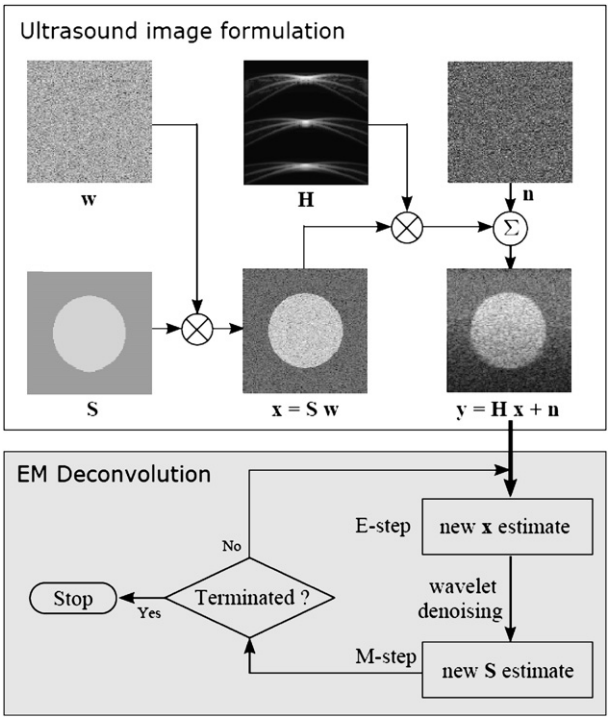

Fig. 13. Diagram showing the key aspects of our deconvolution algorithm. The upper half shows the ultrasound image model ($\mathbf{y} = \mathbf{H}\,\mathbf{x} + \mathbf{n}$) with our interpretation of the structure of the ultrasound reflectivity function ($\mathbf{x} = \mathbf{S}\mathbf{w}$). The lower part is the algorithmic flow chart of the deconvolution itself. Notation: echogenicity ($\mathbf{S}$), random component ($\mathbf{w}$), reflectivity function ($\mathbf{x}$), linear blurring operator or PSF ($\mathbf{H}$), white Gaussian noise ($\mathbf{n}$), and RF ultrasound data ($\mathbf{y}$). The capital letter E in EM and E-step stands for expectation, and M in EM and M-step for maximisation (Ng et al. 2007).

$$\hat{\mathbf{x}} = \left[\mathbf{H}^H\mathbf{H} + \left(\sigma_x^2/\sigma_n^2\right)^{-1}\mathbf{I}_N\right]^{-1}\mathbf{H}^H\mathbf{y} \tag{3}$$

Here, σ_n^2 is the variance of $\mathbf{n}$, σ_x^2 the variance of $\mathbf{x}$, and $\mathbf{I}_N$ the identity matrix with size N. Further, the ratio (σ_x^2/σ_n^2) is collectively known as the signal-to-noise ratio (SNR). The superscript H denotes the Hermitian transpose. We now return to the numerical example. In measurements, we can only estimate an approximate SNR. Therefore, although the exact SNR of this simulation is 23.98 dB, we assume here its estimate was found to be 25 dB. Then, readers can easily calculate an estimate $\hat{\mathbf{x}}\begin{pmatrix}-0.51\\0.51\end{pmatrix}$ according to eqn (3). The estimate is closer to the true reflectivity function $\mathbf{x}\begin{pmatrix}-1\\2\end{pmatrix}$ than the observed ultrasound data $\mathbf{y}\begin{pmatrix}-2.1\\-0.9\end{pmatrix}$: see the ratio of elements, for example, $x_1/x_2 = -0.5$, $\hat{x}_1/\hat{x}_2 = -1$, and $y_1/y_2 = 2.33$. This example illustrates that an initially unfeasible deconvolution problem can be made solvable through regularisation and its solution $\hat{\mathbf{x}}$ is an improvement on the original ultrasound data $\mathbf{y}$.

This numerical example is an extreme case to illustrate the ill-posed nature of the deconvolution process with a non-invertible PSF. However, in reality, the situation is usually more promising. Let's briefly introduce another numerical example with a better PSF:

$\begin{bmatrix}0.1\\4.9\end{bmatrix}=\begin{bmatrix}2&1\\3&4\end{bmatrix}\begin{bmatrix}-1\\2\end{bmatrix}+\begin{bmatrix}0.1\\-0.1\end{bmatrix}$, which has the same **x** as the previous example and noise with the same statistical properties. An interesting aspect of this example is that there is destructive interference occurred in part of the ultrasound data (y_1), whose non-zero status is merely a result of the noise. If a SNR of 25 dB is applied again, one can easily evaluate an estimate. $\hat{\mathbf{x}}\begin{pmatrix}-0.9\\1.9\end{pmatrix}$ Now the solution is very close to the reflectivity function $\mathbf{x}\begin{pmatrix}-1\\2\end{pmatrix}$. See also the ratio of elements: $x_1/x_2 = -0.5$, $\hat{x}_1/\hat{x}_2 = -0.474$, and $y_1/y_2 = 0.020$. Therefore, through deconvolution, it is demonstrated that the original status of the reflectivity function can be restored to a considerable extent, even if there is destructive interference and, hence, effectively no signal is received after beamforming from a part of the ultrasound image.

Instead of using a Gaussian prior for the entire tissue (**x**), we model the tissue reflectivity as the product of microscopically randomised fluctuations (**w**) and a macroscopically smooth tissue-type image called the echogenicity map (**S**) which shares the characteristics of natural images (Ng et al. 2007).

$$\mathbf{x} = \mathbf{S}\,\mathbf{w} \tag{4}$$

See Figure 13 for the formation of **x** in this regard. This formula enables us to control speckle statistics more effectively than the Wiener filter. Here, **w** is a $N \times 1$ complex vector, and **S** is a $N \times N$ diagonal matrix with real non-negative values.

If a zero-mean Gaussian prior is assigned to **w**, then **x** is also observed to be a zero-mean Gaussian when **S** is known. This implies two key procedures in our algorithm. First, when **S** is known, then **x** can be found by using the Wiener filter [eqn (3)]. Second, with **x** found from the first step, if logarithmic operator is applied to eqn (4), then **w** can be treated as additive noise. So, **S** can be determined through a denoising process. Using an expectation-maximisation (EM, see Therrien 1992, p. 285) framework, we can construct an iterative deconvolution strategy alternating between the Wiener filter for **x** (expectation step) and the denoising for **S** (maximisation step).

For denoising, we adopted a wavelet-based algorithm to separate **x** into its **S** and **w** components. We therefore represent the reflectivity function **x** using the dual-tree complex wavelet transform DT-$\mathbb{C}$WT (Kingsbury 1999, 2001), which has been shown to be particularly effective in denoising applications (Sendur and Selesnick 2002).